Department of Physics and Astronomy
Heidelberg University

Bachelor Thesis in Physics
submitted by

Gunho Jason Gabriel Jun

born in Dortmund (Germany)

2023

Simulation of an $Al_{0.73}Ga_{0.27}N/AlN$ Integrated Waveguide Electro-Optic Modulator

This Bachelor Thesis has been carried out by Jason Gabriel Jun at the
Kirchhoff Institute for Physics in Heidelberg
under the supervision of
Prof. Dr. Wolfram Pernice

Abstract

Waveguide-integrated electro-optic phase modulators (EOM) are one of the fundamental building blocks in integrated photonic circuits and can display varying performances depending on material and geometric structure. In this thesis, the values of the optimized geometric parameters for a single $Al_{0.73}Ga_{0.27}N$ waveguide EOM device on 200 nm- and 300 nm-waveguide layer heterostructures are determined. The results are obtained using a simulation based optimization of effective electric field with an attenuation constraint. An estimate phase flip length of $L_\pi^{200\text{nm}} = 12.63$ mm and $L_\pi^{300\text{nm}} = 12.50$ mm is predicted with an applied voltage of $V_{\text{signal}} = 5$ V. An $Al_{0.73}Ga_{0.27}N$ based waveguide thus has the potential to become a platform for integrated photonics and further experimental data using this first configuration will be needed to determine its final performance.

Zusammenfassung

Elektro-optische Phasenmodulatoren (EOM) auf integrierten Wellenleitern sind einer der grundlegenden Bausteine in der integrierten Photonik und können je nach Material und geometrischem Aufbau unterschiedliches Verhalten aufweisen. In dieser Arbeit bestimmen wir die Werte der optimierten geometrischen Parameter für ein einzelnes $Al_{0.73}Ga_{0.27}N$-Wellenleiter-EOM-Bauelement auf der Basis von 200 nm- und 300 nm-Wellenleiterschicht-Heterostrukturen. Die Werte werden durch eine simulationsbasierte Optimierung des effektiven elektrischen Feldes unter der Bedigungen einer geringfügigen Absoprtion ermittelt. Wir berechnen demnach Schätzungswerte der Phasenumdrehungslänge von $L_\pi^{200\text{nm}} = 12.63$ mm und $L_\pi^{300\text{nm}} = 12.50$ mm mit einer angelegten Spannung von $V_{\text{signal}} = 5$ V. Ein $Al_{0.73}Ga_{0.27}N$-basierter Wellenleiter hat somit eine vielversprechende Aussicht, und weitere experimentelle Daten unter Verwendung dieser ersten Konfiguration werden benötigt, um seine endgültige Leistung zu bestimmen.

Contents

1 | Introduction

1.1 Motivation

In recent history, combining research areas such as optics and electronics has given rise to many applied disciplines. A clear example of an emergent branch of optics is the field of integrated optics, or more precisely, integrated photonics. Integrated photonics are inspired by the closely related field of integrated electronics, which similarly deals with the miniaturization of electrical circuits and components. It is the study of miniature optical components on a planar substrate and its combined functionalities with the aim to connect optical devices at the micro-scale by so-called waveguides [1].

Apart from being similar in concept, integrated photonics and integrated electronics share a common steps of fabrication. Therefore, integrated electronics play an important role, as well-established and currently used techniques can be applied to integrated photonics. With increasingly higher circuit density, the industry is reaching a physical bottleneck and requires new technology to fulfill the demand for higher transmission rates and smaller devices. Thanks to its use of optical signals, integrated photonics is becoming ever more relevant for the future of information technology and computer science. In particular, waveguide technology, which describes devices and systems widely used in optical communications, optical computing, optical processing, and optical sensors, is the foundation for solving the imminent physical limitations [1]. To this end, it is of great interest to explore new materials and fabrication procedures to find physically and economically suitable candidates.

1.2 Scope of Thesis

Within the frame of the Munich Quantum Valley Initiative, the research team under the supervision of Professor Wolfram Pernice at the University of Heidelberg is tasked with realizing integrated photonic modulation networks with high precision control of light pulses. The key element of such a network is the electro-optical modulator (EOM) integrated on waveguides. The desired wavelength of the photons is in the ultraviolet (UV) range of 100 nm to 400 nm and requires the use of an appropriate waveguide material. Aluminium Gallium Nitride (AlGaN), which has a large band-gap and consequently low absorption loss in the UV regime [2], will be used in a heterostructure with an Aluminium Nitride (AlN) substrate to support the specific wavelengths in an integrated circuit. Research and experimental data on the electro-optical properties of this material, especially for specific alloy configurations, are limited and subject to further research. The The main objective of this thesis is to find the optimal physical dimensions of an AlGaN waveguide cross-section with an AlN substrate and the optimal arrangement of electrodes to function as an electro-optic phase modulator able to achieve to obtain full phase control at reasonable voltages, which can be used to create destructive interference of photons.

2 | Theory

To understand the physical concepts used in the device, the relevant theory of electrodynamics and solid state physics will be derived and outlined. Vectors are denoted with bold, upright letters, while tensors (including matrices) and scalars (including matrix elements) are denoted with italic letters.

2.1 Light in Dielectric Media

In classical electrodynamics, the most common mathematical description of the electromagnetic theory are the well-known Maxwell-equations which involve the vector-valued, time- and space-dependent *electric field* $\mathbf{E} := \mathbf{E}(t, \mathbf{x})$ and *magnetic flux density* $\mathbf{B} := \mathbf{B}(t, \mathbf{x})$. They are related to each other by the *electric charge density* $\rho := \rho(t, \mathbf{x})$ and the *electric current density* $\mathbf{J} := \mathbf{J}(t, \mathbf{x})$, which are generally time- and space-dependent quantities, and by the *vacuum electric permittivity* ε_0 and the *vacuum magnetic impermeability* μ_0 which both are physical constants with the following values [3, p.44]:

$$\varepsilon_0 \approx 8.8541878128 \cdot 10^{-12}\ \mathrm{F/m} \tag{2.1}$$

$$\mu_0 \approx 1.25663706212 \cdot 10^{-6}\ \mathrm{N/A^2} \tag{2.2}$$

Due to microscopic phenomena inside media, the electromagnetic field gives rise to electric and magnetic dipole moments on a molecular scale. Averaged over the volume of the medium, the distribution of the dipole moment densities can be expressed by the fields $\mathbf{P} := \mathbf{P}(t, \mathbf{x})$ and $\mathbf{M} := \mathbf{M}(t, \mathbf{x})$, often simply referred to as *polarization* and *magnetization*. The divergence of the polarization field and the curl of the magnetization field each contribute to the electric charge

density and the current density respectively. Effectively, this amounts to the superposition of the polarization and magnetization with the electric field and magnetic flux density. The *electric displacement field* $\mathbf{D} := \mathbf{D}(t, \mathbf{x})$ and the *magnetic field* $\mathbf{H} := \mathbf{H}(t, \mathbf{x})$ can thus be defined as [4, p.4]:

$$\mathbf{D} = \varepsilon_0 \mathbf{E} + \mathbf{P}, \tag{2.3}$$

$$\mathbf{H} = \mu_0^{-1} \mathbf{B} - \mathbf{M}. \tag{2.4}$$

The Maxwell-equations in macroscopic form (i.e. inside media) are [1, pp.25-26]:

$$\boldsymbol{\nabla} \cdot \mathbf{D} = \rho_{free}, \tag{2.5}$$

$$\boldsymbol{\nabla} \cdot \mathbf{B} = 0, \tag{2.6}$$

$$\boldsymbol{\nabla} \times \mathbf{E} = -\frac{\partial}{\partial t}\mathbf{B}, \tag{2.7}$$

$$\boldsymbol{\nabla} \times \mathbf{H} = \mathbf{J}_{free} + \frac{\partial}{\partial t}\mathbf{D}, \tag{2.8}$$

where ρ_{free} is the *free electric charge density* and $\mathbf{J}_{free}$ is the *free electric current density*. From this point on, the derivations will be limited to non-magnetic, non-conductive, dielectric media by setting the free charge density, the free current density and the magnetization to zero:

$$\rho_{free} = 0, \tag{2.9}$$

$$\mathbf{J}_{free} = \mathbf{0}, \tag{2.10}$$

$$\mathbf{M} = \mathbf{0}. \tag{2.11}$$

In general, the polarization field $\mathbf{P}$ has a non-linear, inhomogeneous dependence on the electric field $\mathbf{E}$. Using Taylor-expansion, the polarization field can be split into its linear and non-linear part and rewrite equation (2.3) as

$$\mathbf{D} = \varepsilon_0 \mathbf{E} + \mathbf{P} \tag{2.12}$$

$$= \varepsilon_0 \mathbf{E} + \mathbf{P}^L + \mathbf{P}^{NL} \tag{2.13}$$

$$= \varepsilon_0 \mathbf{E} + \varepsilon_0 \chi \mathbf{E} + \mathbf{P}^{NL} \tag{2.14}$$

$$= \varepsilon_0 \left(\mathbb{1} + \chi\right) \mathbf{E} + \mathbf{P}^{NL}, \tag{2.15}$$

where χ is the *electric susceptibility* tensor which is in general of second order and can therefore be represented by a three by three matrix. Because this tensor is symmetric for non-magnetic and transparent materials [5, p.496], it can be diagonalized by choosing the appropriate set of coordinate axes, zeroing all components of the tensor except the diagonal. For low-intensity electric fields the non-linear part of the polarization field $\mathbf{P}^{NL}$ can be neglected, linearizing (2.15) to (2.16).

$$\mathbf{D} = \varepsilon\mathbf{E} \tag{2.16}$$

$$\varepsilon := \varepsilon_0 \left(\mathbb{1} + \operatorname{diag}\left(\chi_1, \chi_2, \chi_2\right)\right) \tag{2.17}$$

Here, the material specific *electric permittivity* tensor ε has been introduced. It is linearly dependent on the electric susceptibility tensor. Using (2.16) and (2.9), the set of differential equations are changed to

$$\boldsymbol{\nabla} \cdot \mathbf{E} = 0, \tag{2.18}$$

$$\boldsymbol{\nabla} \cdot \mathbf{B} = 0, \tag{2.19}$$

$$\boldsymbol{\nabla} \times \mathbf{E} = -\frac{\partial}{\partial t}\mathbf{B}, \tag{2.20}$$

$$\boldsymbol{\nabla} \times \mathbf{B} = \mu_0\varepsilon\frac{\partial}{\partial t}\mathbf{E}. \tag{2.21}$$

The solution to these equations is given by any electromagnetic wave with a propagation speed in each principal axis direction, given by the diagonal elements of the propagation speed tensor $c := (\mu_0\varepsilon)^{-\frac{1}{2}}$. In vacuum, the relative permittivity is equal to one, which defines the vacuum speed of light $c_0 := (\mu_0\varepsilon_0)^{-\frac{1}{2}}$. *refractive index* tensor n is defined as the inverse ratio of the intra-medial propagation speed to the vacuum speed of light:

$$n := c^{-1}c_0 = (\mu_0\varepsilon_0)^{-\frac{1}{2}} (\mu_0\varepsilon)^{\frac{1}{2}} = \left(\varepsilon_0^{-1}\varepsilon\right)^{\frac{1}{2}}. \tag{2.22}$$

This tensor is consequently diagonal and its diagonal elements correspond to the principal refractive indices of the medium. For optically isotropic media, the electric susceptibility is reduced to a scalar quantity, thus reducing the refractive index tensor into a scalar quantity as well.

2.2 Waveguides

The most basic components required for an integrated optical circuit are the previously mentioned waveguides. Waveguides can be understood as micro-scale optical fibres in the sense that they both utilize the same basic physical property of light. A non-exhaustive definition of a waveguide structure would be the combination of a high-index optical medium, i.e. the core, that is extended along the longitudinal direction of light propagation with a surrounding medium, the cladding, that has a lower refractive index than the core. Limiting ourselves to monochromatic planar waves, it can be shown, that the angular frequency ω is conserved across the interface, implying that incident, reflected and transmitted waves all have the same wavelength. Furthermore, due to continuity properties of the electric and magnetic fields, the wave vector of the incident wave and of the transmitted wave must have the same value for the component tangential to the interface. Therefore the well-known Snell's law is given as [6, p.588]

$$\frac{\sin\theta_1}{\sin\theta_2} = \frac{n_2}{n_1}. \tag{2.23}$$

Considering the interface of two media with refractive indices n_1 and n_2 with $n_1 > n_2 > 0$, setting the angle of refraction to $\theta_2 = 90°$ implies that there is a *critical angle* θ_c at which there is no wave propagating into the lower index medium, as expressed in (2.24) [6, p.589].

$$\frac{\sin\theta_c}{\sin(90°)} = \frac{n_2}{n_1} \quad \Rightarrow \quad \theta_c = \arcsin\frac{n_2}{n_1} \tag{2.24}$$

Light inside a medium with a refractive index higher than that of its surrounding media will thus be confined inside said medium due to total internal reflection. This allows for transmission of light over distances characteristic for the respective size-scale [1, p.7]. While optics and micro-optics work with fibres of sizes on the scale of 10^{-2} to 10^{-3} metres, waveguides, working at size-scales three orders of magnitude smaller, can't be described through ray optics and require the description of light as electromagnetic waves propagating through solid media [1, p.24]. An in-depth wave analysis of waveguides goes beyond the scope of this thesis, but can be found in the referenced sources [1, 4, 5, 7]. Ultimately,

the task is to solve the Maxwell-equations with the given boundary conditions, where the resulting solutions are the confined modes inside the waveguide and are shaped by the waveguide geometry.

2.3 Electro-Optic Modulators

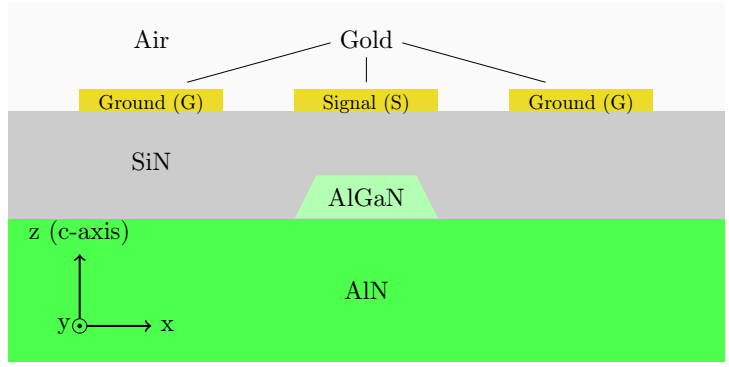

(a) Cross-sectional view

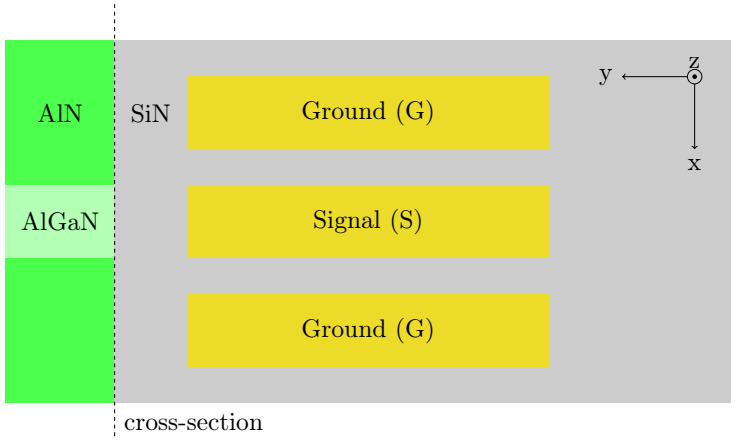

(b) Vertical view with cross-section line

Figure 2.1: Schematic views of the final waveguide EOM arrangement viewed a) as a cross-section and b) from above.

The main device for this setup is an *electro-optic phase modulator*, which modulates the phase by making use of the electro-optic effect. The electro-optic effect is the change in refractive index of a material induced by the presence of an external, locally static electric field, which is called the *modulation field*. In the case of a static or low-frequency modulation field $\mathbf{E}^{\mathrm{mod}}$ that has sufficiently high intensity, the polarization field cannot be assumed to be linearly dependent.

Instead, an electro-optically induced change in the electric permittivity tensor for the optical electric field $\mathbf{E}^{\text{opt}}$ has to be considered:

$$\mathbf{D} \quad = \quad \varepsilon \mathbf{E}^{\text{opt}} = \left[\varepsilon + \Delta\varepsilon\left(\mathbf{E}^{\text{mod}}\right)\right]\mathbf{E}^{\text{opt}}. \tag{2.25}$$

In absence of the modulation field, the (intrinsic) electric permittivity tensor ε of the medium is diagonal in the coordinate system that is defined by the intrinsic principal axes. The *relative impermeability tensor* η is then defined as

$$\eta = \varepsilon_0 \varepsilon^{-1}. \tag{2.26}$$

This tensor is again diagonal, because the intrinsic permittivity tensor is diagonal. An external field induces an additional polarization field inside the medium, influencing the susceptibility tensor, and thus the relative impermeability tensor. Specifically, the intrinsic electric impermeability tensor η is complemented by the generally non-diagonal, electro-optically induced second order tensor $\Delta\eta\left(\mathbf{E}^{\text{mod}}\right)$, resulting in the total electric impermeability tensor $\eta^{eo}\left(\mathbf{E}^{\text{mod}}\right)$ as shown in (2.27). For non-centrosymmetric media, the most significant change to each element of the relative impermeability tensor is caused by the *linear electro-optic effect*, also known as the *Pockel's effect*. The change in relative impermeability is most commonly described by the electro-optically induced impermeability tensor $\Delta\eta$, where each element is a linear combination of the modulation field vector $\mathbf{E}^{\text{mod}}$ with the *linear electro-optic (Pockel's) coefficients* as scalar factors [4, p.240]:

$$\eta^{eo} \quad = \quad \eta + \Delta\eta \tag{2.27}$$

$$\Delta\eta_{ij} \quad = \quad \sum_{k=1}^{3} r_{ijk} E_k^{\text{mod}}. \tag{2.28}$$

Using the definition given in (2.26), the change in impermeability tensor can be translated into change in permittivity tensor as shown in (2.30).

$$\Delta\varepsilon \quad = \quad -\varepsilon_0^{-1}\varepsilon\Delta\eta\varepsilon \tag{2.29}$$

$$\Delta\varepsilon_{ij} \quad = \quad -\varepsilon_0 n_i^2 n_j^2 \sum_{k=1}^{3} r_{ijk} E_k^{\text{mod}} \tag{2.30}$$

Since the linear electro-optic coefficient tensor is symmetric in its first two indices, it can be reduced by contracting the redundant index pairs into one index, allowing for a matrix representation of the Pockel's coefficients:

$$\begin{pmatrix} r_{11k} & r_{12k} & r_{13k} \\ r_{21k} & r_{22k} & r_{23k} \\ r_{31k} & r_{32k} & r_{33k} \end{pmatrix} = \begin{pmatrix} r_{1k} & r_{6k} & r_{5k} \\ r_{6k} & r_{2k} & r_{4k} \\ r_{5k} & r_{4k} & r_{3k} \end{pmatrix} \quad \forall k \in 1,2,3 \tag{2.31}$$

$$\Rightarrow \tilde{r} = \begin{pmatrix} r_{11} & r_{12} & r_{13} \\ r_{21} & r_{22} & r_{23} \\ r_{31} & r_{32} & r_{33} \\ r_{41} & r_{42} & r_{43} \\ r_{51} & r_{52} & r_{53} \\ r_{61} & r_{62} & r_{63} \end{pmatrix}. \tag{2.32}$$

In a waveguide structure, the geometric arrangement and the distribution of the optical field of the mode influence the overall effect the modulation field has on the mode. The distribution of the modulation field across the optical mode is generally not uniform. The electro-optic effect inside a waveguide can be calculated using the coupled-mode theory. For single mode waveguides, the change in the propagation constant of the mode is equal to the self-coupling coefficient [4, p.260]

$$\Delta\beta_\nu = \kappa_{\nu\nu} = -\omega \int_A \overline{\mathbf{E}^{\mathrm{opt}}} \Delta\varepsilon \mathbf{E}^{\mathrm{opt}} d\boldsymbol{x}. \tag{2.33}$$

The total electro-optically induced phase shift of this mode over length L of the modulator is then given by the equation given by [4, p.261]

$$\Delta\theta = \Delta\beta_\nu L. \tag{2.34}$$

For full phase control, the EOM must be able to induce a total phase flip. To achieve a phase flip, the phase shift in (2.34) is set to $\Delta\theta = \pi$ and the equation is rearranged to obtain the modulation length

$$L_\pi = \frac{\pi}{\Delta\beta_\nu}. \tag{2.35}$$

2.4 AlGaN

The material used for the waveguides in this project is *Aluminium Gallium Nitride* (AlGaN). AlGaN is an alloy of *Aluminium Nitride* (AlN) and *Gallium Nitride* (GaN). It thus belongs to the group of III-V-semiconductor materials and has a Wurtzite crystal structure which is dihexagonal pyramidal [8]. A visualization of the atomic structure in Wurtzite crystals is given in Figure 2.2. Wurtzite crystal are uniaxial crystals and therefore only have two principal re-

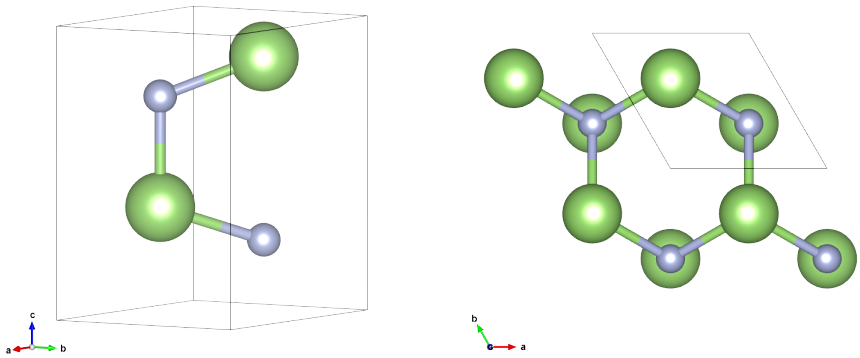

(a) (b)

Figure 2.2: Wurtzite Crystal structure (Gallium or Aluminium atoms in green, Nitrogen atoms in blue) shown a) in a unit cell and b) viewed from c-axis.

fractive indices. The refractive index for components perpendicular to the c-axis, i.e. for ordinary rays, is $n_o = n_1 = n_2$ and the refractive index for extraordinary rays is $n_e = n_3$. The corresponding crystallographic point symmetry group in the Hermann-Mauguin notation is $6mm$. Due to this point symmetry, the electro-optic coefficient matrix of AlGaN is reduced to only five elements with 3 independent coefficients r_{13}, r_{33} and r_{42} [4, p.244]. The electro-optic coefficient

matrix reduces to

$$\tilde{r}^{\mathrm{AlGaN}} = \begin{pmatrix} 0 & 0 & r_{13} \\ 0 & 0 & r_{13} \\ 0 & 0 & r_{33} \\ 0 & r_{42} & 0 \\ r_{42} & 0 & 0 \\ 0 & 0 & 0 \end{pmatrix}, \tag{2.36}$$

yielding the explicit expression for the electro-optically induced relative permittivity tensor with

$$\Delta\varepsilon = -\varepsilon_0 \begin{pmatrix} n_o^4 r_{13} E_3^{\mathrm{mod}} & 0 & n_o^2 n_e^2 r_{42} E_1^{\mathrm{mod}} \\ 0 & n_o^4 r_{13} E_3^{\mathrm{mod}} & n_o^2 n_e^2 r_{42} E_2^{\mathrm{mod}} \\ n_o^2 n_e^2 r_{42} E_1^{\mathrm{mod}} & n_o^2 n_e^2 r_{42} E_2^{\mathrm{mod}} & n_e^4 r_{33} E_3^{\mathrm{mod}} \end{pmatrix}. \tag{2.37}$$

Only the transverse electrical modes which have in-plane electrical field components are relevant, i.e. $\mathbf{E}^{\mathrm{opt}} = \mathbf{E}_{\mathrm{TE}}^{\mathrm{opt}} = E_1^{\mathrm{opt}} \hat{\mathbf{e}}_1$. The change in propagation constant thus simplifies to

$$\begin{aligned} \Delta\beta_{\mathrm{TE}} &= -\omega \int_A \overline{\mathbf{E}_{\mathrm{TE}}^{\mathrm{opt}}} \Delta\varepsilon \mathbf{E}_{\mathrm{TE}}^{\mathrm{opt}} d\boldsymbol{x} && (2.38)\\ &= -n_o^4 r_{13} \varepsilon_0 \omega \int_A E_3^{\mathrm{mod}} \left|E_1^{\mathrm{opt}}\right|^2 d\boldsymbol{x} && (2.39)\\ &= -n_o^4 r_{13} \frac{\omega^2 \mu_0 \varepsilon_0}{2\beta_{\mathrm{TE}}} \frac{2\beta_{\mathrm{TE}}}{\omega\mu_0} \int_A E_3^{\mathrm{mod}} \left|E_1^{\mathrm{opt}}\right|^2 d\boldsymbol{x} && (2.40)\\ &\approx -n_o^4 r_{13} \frac{\pi}{n_o \lambda} E_{\mathrm{eff}}^{\mathrm{mod}} && (2.41)\\ &= -n_o^3 r_{13} \frac{\pi}{\lambda} E_{\mathrm{eff}}^{\mathrm{mod}}, && (2.42) \end{aligned}$$

where the effective modulation field is defined as the cross-sectional integral of the modulation field component overlap [4, p.261]:

$$E_{\mathrm{eff}}^{\mathrm{mod}} = \frac{2\beta_{\mathrm{TE}}}{\omega\mu_0} \int_A E_3^{\mathrm{mod}} \left|E_1^{\mathrm{opt}}\right|^2 d\boldsymbol{x} = \frac{\int_A E_3^{\mathrm{mod}} \left|E_1^{\mathrm{opt}}\right|^2 d\boldsymbol{x}}{\int_A \left|E_1^{\mathrm{opt}}\right|^2 d\boldsymbol{x}}. \tag{2.43}$$

By inserting $\Delta\beta_{\mathrm{TE}}$ from (2.42) into (2.35), the modulation length can be calculated from the effective modulation field:

$$L_\pi = \frac{\lambda}{-n_o^3 r_{13} E_{\mathrm{eff}}^{\mathrm{mod}}}. \tag{2.44}$$

3 | Study

3.1 Geometric Structure

The following section will briefly present the geometric arrangement of the EOM used during the course of the simulations and the reasons for choosing this setup. The heterostructures for the waveguides that were manufactured are out-of-plane c-axis oriented epitaxial layers of 200 nm or 300 nm of $Al_{0.73}Ga_{0.27}N$ on 1000 nm of AlN on 430 µm sapphire. The manufactured heterostructure is shown schematically in Figure 3.1. The c-axis of the AlGaN layer is oriented

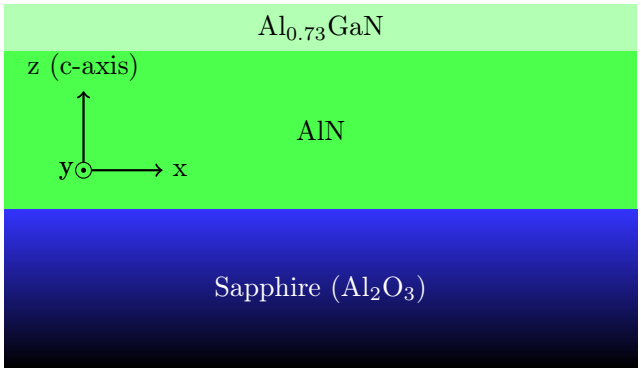

Figure 3.1: Cross-section of the AlGaN/AlN heterostructure.

orthogonal to the substrate plane. The modulation field has to be parallel to the c-axis which requires an electrode setup that introduces an effective out-of-plane electric field. This is achieved by a symmetric arrangement of ground-signal-ground (G-S-G) gold pads on top of a silicon nitride (SiN) cladding layer. The arrangement that was chosen has horizontally placed electrodes all on top of the cladding layer as opposed to one inside the cladding, below the waveguide and

one on top of the cladding. The latter arrangement would ensure a nearly homogeneous field distribution across the waveguide, but would be more difficult to fabricate due to the increased number of fabrication steps. With the horizontal arrangement, a minor compromise is taken in effective modulation field for a much simpler fabrication procedure. The gold pad electrodes are absorbent at UV wavelengths and can cause attenuation of the mode inside the waveguide. The key quantity to be observed is $E_{\text{eff}}^{\text{mod}}$. The geometry of the waveguide is limited by the layer thickness in the hetero-structure and by the post-etching waveguide side angle to the substrate, where a side angle of approximately 30° is a realistic prediction for the final waveguide geometry. This leaves the width of the waveguide w_{wg} as a variable parameter. The G-S-G electrode setup is deposited on top of the level cladding layer and aligned with the symmetry axis of the waveguide cross-section. The geometry and placement of the electrodes are then described by the height of the cladding layer h_{cl}, which is the distance of the electrodes to the substrate, and the width of the gap d_{gap} between each of the electrodes, which principally influences the shape of the electric field. A cross-sectional view of the schematic arrangement with the variable parameters is given in Figure 3.2.

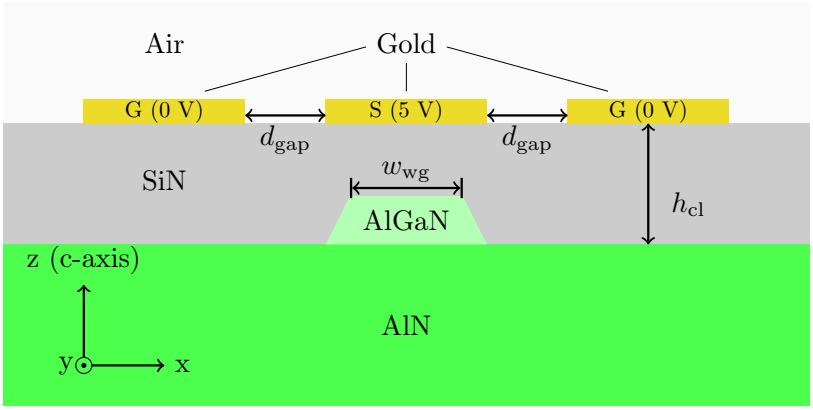

Figure 3.2: Cross-section of the schematic final waveguide EOM arrangement with parameters $w_{\text{wg}} \sim 200$ nm, $h_{\text{cl}} \sim 700$ nm and $d_{\text{gap}} \sim 300$ nm.

3.2 Materials

The lasers used for the final waveguide structure have a wavelength of $\lambda = 317\,\text{nm}$ as required by the project framework. The refractive indices for the gold electrode pads at this wavelength is $n_{\text{Au}} = 1.5365$ with and extinction coefficient of $k_{\text{Au}} = 1.8962$ [9]. The silicon nitride cladding layer has a refractive index of $n_{\text{SiN}} = 2.1493$ with no absorption [10]. According to the wafer manufacturer, both the waveguide and substrate material show no relevant absorption for light at this wavelength. The refractive index for ordinary rays n_o of $\text{Al}_{0.73}\text{Ga}_{0.27}\text{N}$ and AlN are provided by the manufacturer and shown in Figure 3.3. The re-

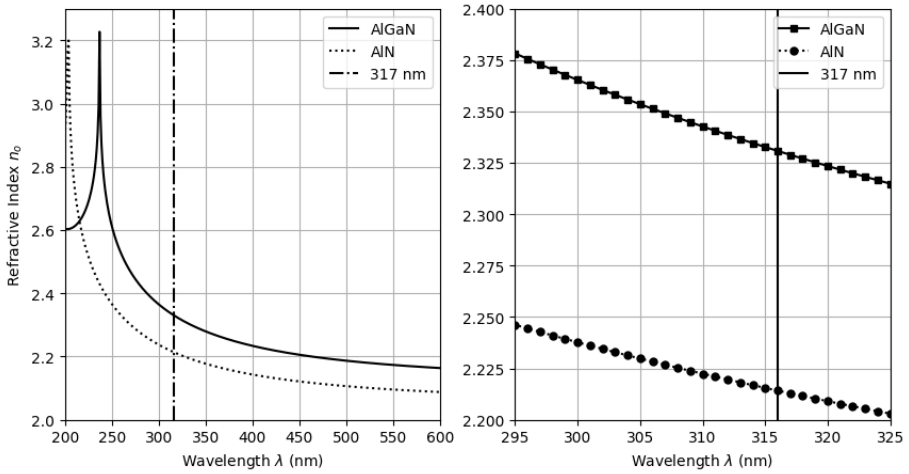

Figure 3.3: Refractive indices for the ordinary ray in $\text{Al}_{0.73}\text{Ga}_{0.27}\text{N}$ and AlN.

fractive indices corresponding to a wavelength of 317 nm are $n_{\text{AlN}} = 2.214198$ and $n_{\text{AlGaN}} = 2.330808$. Since the fundamental mode (TE mode) has in-plane polarization, which is always perpendicular to the optical axis, birefringence can be excluded and thus no knowledge about the refractive index n_e for extraordinary rays is required. The critical angle for total internal reflection at the AlGaN/AlN interface is then given by (2.24) as $\theta_c \approx 71.80°$. Experimental data on the electro-optic coefficients of AlGaN with the specific Aluminium to Gallium ratio could not be found. This limits the scope of this thesis to the optimization of geometric parameters with respect to indicative quantities such as the attenuation loss and the effective modulation field inside the waveguide.

3.3 Single Mode Propagation

When examining a 3D waveguide construction, it is crucial to understand which types of electromagnetic waves are permitted to propagate at a certain frequency. These modes are fully defined by the global complex-valued propagation constants and the space distributions of all three components of the electric field. For configurations with arbitrary shape and material combinations which include typical integrated waveguides, there are generally no analytic solutions available, which necessitates the use of numeric mode analysis. For a given wavelength, the mode analysis finds out-of-plane wave solutions of the Helmholtz equation for the given geometry by utilizing an eigenvalue solver and the finite element method (FEM) [11]. The mode analysis will be done using the simulation software *COMSOL Multiphysics 6.0* [12]. To achieve single mode

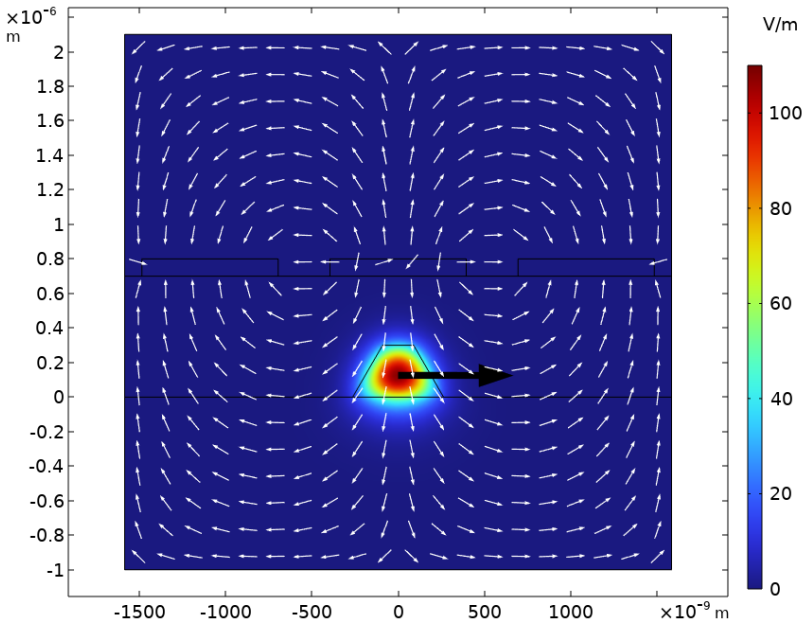

Figure 3.4: Cross-sectional view of the AlGaN-based EOM waveguide structure with single mode propagating optical field distribution, simulated with initial geometric parameters. The mode polarization is represented by the black arrow in the center of the waveguide and the external modulation vector field is given by the white arrows.

propagation, the cut-off width at which only a single mode can propagate inside the waveguide cross-section must be found. In the software, the mode analysis

study module searches for four eigenmodes in the vicinity of the refractive index of AlGaN, while sweeping over different waveguide widths. The eigenvalue solver computes the four eigenmodes whose effective mode indices are closest to the input refractive index in absolute value. Since the value of the effective mode index must be in between the refractive indices of AlGaN, the substrate and the cladding [1, p.66], a cut-off width of the waveguide for single mode propagation can be determined.

3.4 Attenuation and Effective Modulation Field

The waveguide width is now fixed at the highest sweeping point value below the cut-off width and proceed with the simulations needed to determine the optimal electrode setup. The outer two electrodes are set to $V_0 = 0$ V and the center electrode is set to $V_{\text{signal}} = 5$ V. The electrostatic field distribution for different geometric setups of the integrated waveguide EOM is computed. The goal is to maximize the effective modulation field inside the waveguide while maintaining attenuation losses below 0.01 dB/cm. Since the main absorption is due to the gold electrodes, the most significant change on attenuation loss can be achieved by changing the overall relative position of the electrodes. To simulate this, a sweep over a range of cladding layer heights is simulated and both the attenuation loss and effective modulation field at each sweeping point are computed. With the fixed cladding layer height, a sweep over the width of the electrode gap to change the electro-static field distribution.

4 | Results

4.1 Waveguide Width

The simulations commence with as sweep of the waveguide width ranging from 200 nm to 400 nm in steps of 10 nm in heterostructure 1 (200 nm-AlGaN) and from 50 nm to 250 nm in steps of 10 nm for heterostructure 2 (300 nm-AlGaN). Figure 4.1a and 4.1b are plots of the effective mode indices for of all four solutions as a function of the simulated waveguide width. In both figures the upper

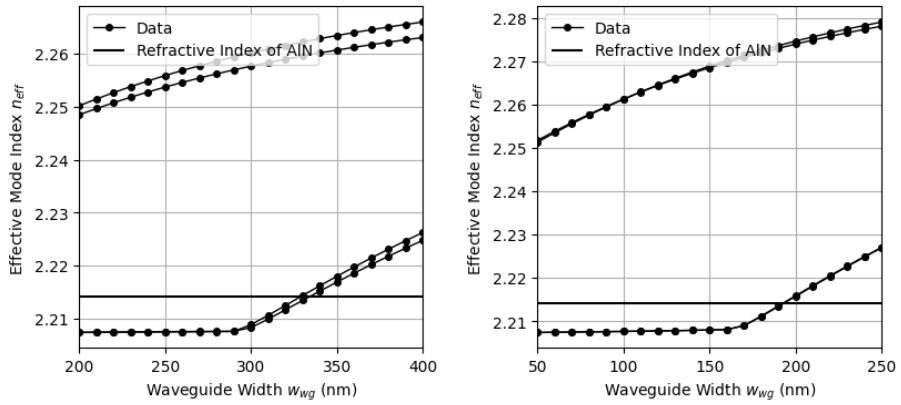

(a) 200 nm AlGaN (b) 300 nm AlGaN

Figure 4.1: The effective mode indices corresponding to the four solutions from the simulated sweep of waveguide widths for a) the 200 nm AlGaN-Layer heterostructure and b) the 300 nm AlGaN-Layer heterostructure.

two lines correspond to the TE- and TM- mode of a single mode propagation, while the lower two correspond to first TE- and TM-mode of the multi-mode propagation. Based on the simulation points, a cut-off waveguide width for single mode propagation of 330 nm (200nm-AlGaN) and 190 nm (300nm-AlGaN)

is chosen.

4.2 Cladding Layer Height

With the fixed waveguide geometry, a sweep of the cladding layer height h_{cl} ranging from 500 nm to 1000 nm in steps of 10 nm for both heterostructure types is simulated. In Figure 4.2a and 4.2b, the attenuation and the effective modulation field are plotted as a function of h_{cl} for the respective heterostructures. The simulated values suggest a qualitatively inverse relationship between the

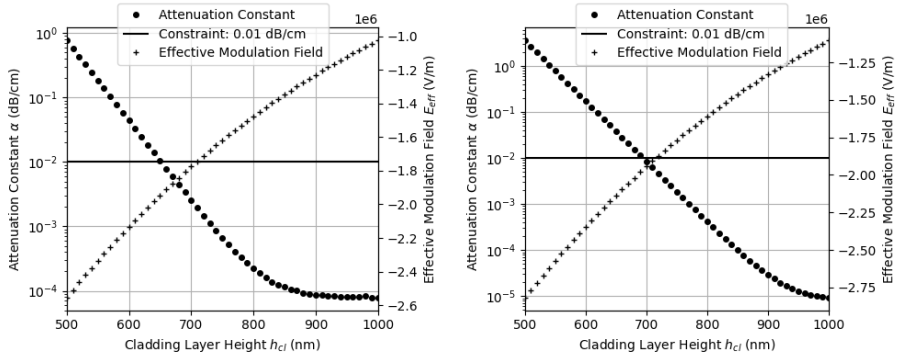

(a) 200 nm AlGaN (b) 300 nm AlGaN

Figure 4.2: The effective modulation field and attenuation constants in logarithmic scale for the simulated sweep of cladding layer widths for a) the 200 nm AlGaN-Layer heterostructure and b) the 300 nm AlGaN-Layer heterostructure.

attenuation and the effective modulation field. The attenuation decreases exponentially, but stagnates at around 10^{-5} dB/cm around $h_{\mathrm{cl}} = 1000$ nm, while the effective modulation field monotonously decreases in absolute value for increasing values of h_{cl}. We choose a cladding layer height of $h_{\mathrm{cl}} = 660$ nm (200nm-AlGaN) and $h_{\mathrm{cl}} = 700$ nm (300nm-AlGaN) at which the attenuation remains below 0.01 dB/cm to maximize the effective modulation field.

4.3 Electrode Gap Width

Finally, a sweep of electrode gap width d_{gap} for each heterostructure type is simulated with widths ranging from 50 nm to 2000 nm in steps of 50 nm. Figure 4.3a shows the effective electric field and the attenuation in logarithmic scale as

a function of d_{gap}. The data suggests that the gap width has negligible effects on

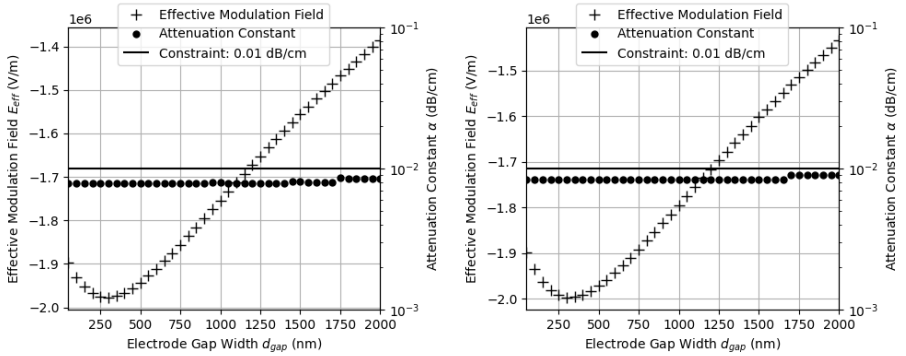

(a) 200 nm AlGaN (b) 300 nm AlGaN

Figure 4.3: The effective modulation field and attenuation constants for the simulated sweep of electrode gap widths for a) the 200 nm AlGaN-Layer heterostructure and b) the 300 nm AlGaN-Layer heterostructure.

the attenuation, staying below the 0.01 dB/cm threshold over the entire sweeping range. The effective modulation field reaches a maximum absolute value of around $E_{\text{eff}}^{\text{mod}} = 1.98$ MV/m (200nm-AlGaN) and $E_{\text{eff}}^{\text{mod}} = 2.00$ MV/m (300nm-AlGaN) for values of $d_{\text{gap}} = 300$ nm in both heterostructures. These values are considered to be the maximum attainable value of the effective modulation field with this setup. Figure 4.4 shows a plot of the cross-sectional optical field distribution and external modulation field surface over the final EOM waveguide geometry for both heterostructure types.

4.4 Phase Flip Length Estimate

An order-of-magnitude estimate for the phase flip modulator length L_π as a function of the r_{13} coefficient's order of magnitude is given with (2.44). The resulting scaling values are given in (4.1) (200nm-AlGaN) and (4.2) (300nm-AlGaN) with r_{13} in units of pm/V.

$$L_\pi^{200} \approx 1.263 \cdot 10^{-2} \cdot \left(\frac{r_{13}}{\text{pm/V}}\right)^{-1} \text{m} \sim 10^{-2} \cdot \mathcal{O}\left(\frac{r_{13}}{\text{pm/V}}\right)^{-1} \text{m} \quad (4.1)$$

$$L_\pi^{300} \approx 1.250 \cdot 10^{-2} \cdot \left(\frac{r_{13}}{\text{pm/V}}\right)^{-1} \text{m} \sim 10^{-2} \cdot \mathcal{O}\left(\frac{r_{13}}{\text{pm/V}}\right)^{-1} \text{m} \quad (4.2)$$

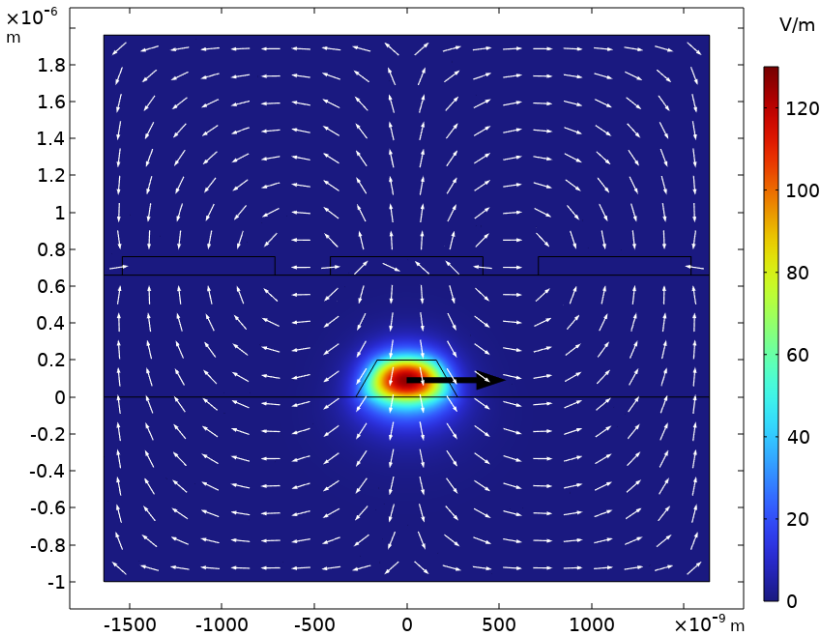

(a) 200 nm AlGaN

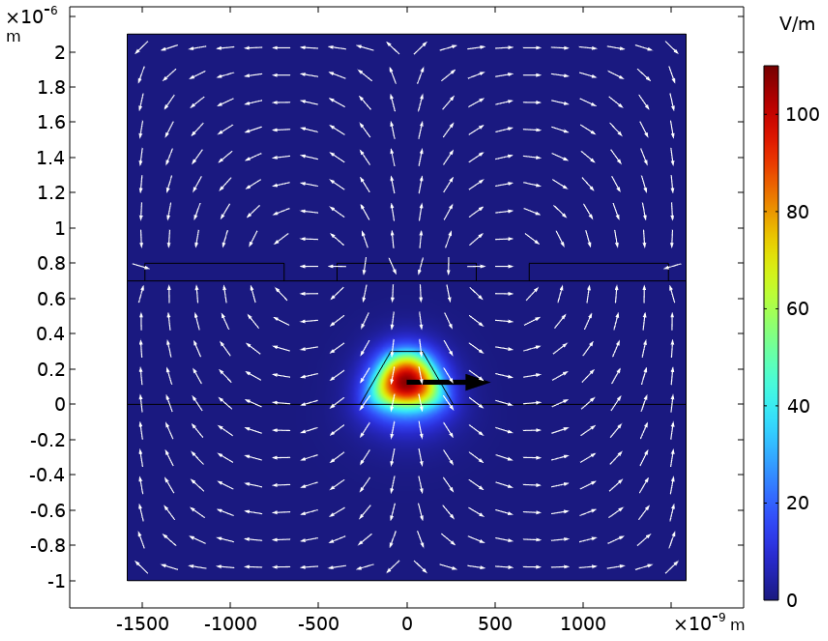

(b) 300 nm AlGaN

Figure 4.4: Cross-sectional view of the AlGaN-based EOM waveguide structure with single mode propagating optical field distribution for the optimized geometric parameters in a) 200nm-AlGaN and b) 300nm-AlGaN. The mode polarization is represented by the black arrow in the center of the waveguide and the external modulation vector field is given by the white arrows.

5 | Conclusion

5.1 Summary

The resulting optimal values for a simulated EOM structure with an applied voltage of 5 V and electro-optic coefficient r_{13} on the order of 1 pm/V are $L_\pi^{200\text{nm}} = 12.63$ mm for waveguides etched from 200 nm AlGaN-layer heterostructures and $L_\pi^{300\text{nm}} = 12.50$ mm for waveguides etched from 300 nm AlGaN-layer heterostructures. Table 5.1 is a summary of the optimal geometric parameter values, the resulting effective modulation field strength and the phase flip length estimate for $r_{13} \sim 1$ pm/V for heterostructure 1 (200 nm AlGaN-layer) and heterostructure 2 (300 nm AlGaN-layer). The given results have to be seen as a first guidance for further characterization. With an estimated required modulation length on centimeter scale, the final EOM structure would have to be rather long. This length can vary depending on the upper support limit of the applied modulation voltage and the exact values of the relevant electro-optic coefficient, which are subject to characterization subsequent to this thesis.

Table 5.1: Values of optimal geometric parameters for AlGaN EOM arrangement with corresponding effective modulation field and estimated phase flip length assuming $r_{13} \sim 1$pm/V.

Parameter	Heterostructure	
	1	2
AlGaN Layer Height (nm)	200	300
Waveguide Width w_{wg} (nm)	330	190
Cladding Layer Height h_{cl} (nm)	660	700
Electrode Gap Width d_{gap} (nm)	300	300
Effective Modulation Field $E_{\text{eff}}^{\text{mod}}$ (MV/m)	1.98	2.00
Phase Flip Length Estimate L_π (mm)	12.63	12.50

5.2 Outlook

Fabrication of the integrated EOM structure will include the etching procedure for the waveguide structure, the deposition of the cladding layer and the placement of the gold pad electrodes. For the etching procedure, different recipes may have to be looked into to find the optimal result in terms of precision and degree of control on the final waveguide geometry. With regards to the cladding layer, the silicon oxide layer can be deposited using plasma-enhanced chemical vapor deposition (PECVD) [10] which is expected to achieve very high rates of deposition with high film quality with regards to roughness and layer defects. Impurities inside the SiO_2 layer resulting from the PECVD procedure can cause increased absorption from the cladding layer, but are expected to be compensated by the very high mode confinement of the light inside the waveguide. Outside of the optimized parameters, other EOM structures and additional geometric parameters could be investigated with regards to better modulation effects, but have not been considered in this thesis. A vertical ground-waveguide-signal electrode arrangement as mentioned in Section 3.1 could yield higher values for the effective modulation field and thus a shorter modulation length, but would involve a more complicated fabrication process.

Post-fabrication objectives will include experimental measurements of the transmission rate, of the phase modulation length per applied voltage, and of the electro-optic coefficients of the AlGaN. The content and results of this thesis may in this regard be seen as a first feasibility evaluation on AlGaN wavguide EOM structures.

Bibliography

[1] G. Lifante, *Integrated Photonics: Fundamentals*, 1st ed. Wiley, Jan. 2003. [Online]. Available: https://onlinelibrary.wiley.com/doi/book/10.1002/0470861401

[2] D. Li, K. Jiang, X. Sun, and C. Guo, "AlGaN photonics: recent advances in materials and ultraviolet devices," *Adv. Opt. Photon.*, vol. 10, no. 1, p. 43, Mar. 2018. [Online]. Available: https://opg.optica.org/abstract.cfm?URI=aop-10-1-43

[3] E. Tiesinga, P. J. Mohr, D. B. Newell, and B. N. Taylor, "CODATA recommended values of the fundamental physical constants: 2018," *Rev. Mod. Phys.*, vol. 93, no. 2, p. 025010, Jun. 2021. [Online]. Available: https://link.aps.org/doi/10.1103/RevModPhys.93.025010

[4] J.-M. Liu, *Photonic Devices*. Cambridge University Press, Jun. 2009.

[5] R. W. Boyd, "The Electrooptic and Photorefractive Effects," in *Nonlinear Optics*. Elsevier, 2020, pp. 495–522. [Online]. Available: https://linkinghub.elsevier.com/retrieve/pii/B9780128110027000205

[6] M. Bartelmann, B. Feuerbacher, T. Krüger, D. Lüst, A. Rebhan, and A. Wipf, *Theoretische Physik*. Berlin, Heidelberg: Springer Berlin Heidelberg, 2015. [Online]. Available: https://link.springer.com/10.1007/978-3-642-54618-1

[7] L. Chrostowski and M. E. Hochberg, *Silicon photonics design*. Cambridge ; New York: Cambridge University Press, 2015.

[8] M. Soltani, R. Soref, T. Palacios, and D. Englund, "AlGaN/AlN integrated photonics platform for the ultraviolet and visible spectral range," *Opt. Express*, vol. 24, no. 22, p. 25415, Oct. 2016. [Online]. Available: https://opg.optica.org/abstract.cfm?URI=oe-24-22-25415

[9] P. B. Johnson and R. W. Christy, "Optical Constants of the Noble Metals," *Phys. Rev. B*, vol. 6, no. 12, pp. 4370–4379, Dec. 1972. [Online]. Available: https://link.aps.org/doi/10.1103/PhysRevB.6.4370

[10] L. Y. Beliaev, E. Shkondin, A. V. Lavrinenko, and O. Takayama, "Optical, structural and composition properties of silicon nitride films deposited by reactive radio-frequency sputtering, low pressure and plasma-enhanced chemical vapor deposition," *Thin Solid Films*, vol. 763, p. 139568,

Dec. 2022. [Online]. Available: https://linkinghub.elsevier.com/retrieve/pii/S0040609022004710

[11] Yankin, Sergey, "Mode Analysis for Electromagnetic Waveguides in COMSOL®," Jul. 2022. [Online]. Available: https://www.comsol.de/blogs/mode-analysis-for-electromagnetic-waveguides-in-comsol/

[12] COMSOL AB, "COMSOL Multiphysics®." [Online]. Available: www.comsol.com

Acknowledgements

At this point, I want to express my sincere gratitude to Professor Wolfram Pernice for giving me the opportunity to work in his research group for my thesis and get acquainted with integrated photonics, and to Professor Lauriane Chomaz for agreeing to be the second examiner for this thesis.

I would also like to thank Philipp Schultzen and Klara Maria Meyer-Hermann for their personal care, and their professional guidance at every step during this thesis, including the final revision.

I am very thankful for Dr. Simone Ferrari sharing his knowledge and years of experience with me, providing me with the necessary sources and information.

Finally, I thank all members of the Neuromorphic Quantumphotonics group, especially Julius Römer and Oliver Page, for their professional input in the group meetings and for their emotional support.

Erklärung

Ich versichere, dass ich diese Arbeit selbstständig verfasst und keine anderen als die angegebenen Quellen und Hilfsmittel benutzt habe.

Heidelberg, den 1. März 2023,

Gunho Jason Gabriel Jun